# An Automatic Radiometric Cross-Calibration Method for Wide-Angle Medium-Resolution Multispectral Satellite Sensor Using Landsat Data

Jun Lu, Tao He, *Member, IEEE*, Shunlin Liang, *Fellow, IEEE*, and Yongjun Zhang

***Abstract*— Radiometric calibration of the medium-resolution satellite data is critical for monitoring and quantifying changes in the Earth's environment and resources. Many medium-resolution satellite sensors have irregular revisits and, sometimes, have a large difference in illumination viewing geometry compared with a reference sensor, posing a great challenge for routine cross-calibration practices. To overcome these issues, this study proposed a cross-calibration method to calibrate medium-resolution multispectral data. The Chinese Gaofen-4 (GF-4) panchromatic and multispectral sensor (PMS) data with large viewing angles were used as the test data, and Landsat-8 operational land imager (OLI) data were used as the reference data. A bidirectional reflectance distribution function (BRDF) correction method was proposed to eliminate the effects of differences in illumination viewing geometry between GF-4 and Landsat-8. The validation using concurrent image shows that the mean relative error (MRE) of cross calibration is less than 6.65%. Validation using ground measurements shows that our calibration results have an improvement of around 14.8% compared with the official released calibration coefficients. The time series cross calibration reveals that, without the requirements of simultaneous nadir observations (SNOs), our calibration activities can be carried out more often in practice. Gradual and continuous radiometric sensor degradation is identified with the monthly updated calibration coefficients, demonstrating the reliability and importance of the timely cross calibration. Besides, the cross-calibration approach does not rely on any specific calibration site, and the difference in illumination viewing geometry can be well considered. Thus, it can be easily adapted and applied to other optical satellite data.**

***Index Terms*— Bidirectional reflectance distribution function (BRDF), Gaofen-4 (GF-4), Landsat-8, radiometric calibration.**

## I. Introduction

RADIOMETRIC calibration is the conversion from satellite recorded digital numbers to values with absolute units of at-sensor radiance for optical bands and brightness temperatures for thermal bands [1]. Frequent sensor calibration is critical for change detection, time series analysis, and quantitative retrieval of biogeophysical properties with remote sensing data [2]. However, for a sensor without an onboard calibration system, the calibration is usually taken using *in situ* measurements obtained from fixed calibration sites [3]. Because of its high time consumption, labor intensity, and cost, field-based calibration activities are carried out at a low frequency (mostly once a year), thus making it difficult to track the sensor degradation [3], which is one of the major challenges using data without the onboard calibration system.

Radiometric cross calibration of in-orbit sensors is an essential technique to ensure the calibration frequency of remote sensing data and the radiometric consistency of different sensors [1]. It uses well-calibrated in-orbit satellite data as a reference to cross calibrate the target sensor data [2], [4]–[6]. A variety of cross-calibration methods have been applied to the Earth observation data. For example, Angal *et al*. [7] used the near-simultaneous image pairs of the Moderate Resolution Imaging Spectroradiometer (MODIS) and Landsat-7 Enhanced Thematic Mapper Plus (ETM+) over a pseudoinvariant calibration site to cross calibrate the Landsat-7 ETM+ data. Farhad *et al*. [8] used the near-nadir view and cloud-free image pairs over six pseudoinvariant calibration sites located in Africa to carry out the cross calibration of the Landsat-8 operational land imager (OLI) and the Sentinel-2A multispectral instrument (MSI). A basic requirement of classic cross calibration is that observations from the target sensor and reference sensor use the same ground target, spectral band, overpass time, and illumination viewing geometry [9].

However, it is unlikely to satisfy all of the above requirements in practice. The reference sensor and target sensor may have a difference in spectral and illumination viewing geometry. The difference will cause uncertainties in cross calibration. The spectral difference is related to their spectral range and relative spectral responses (RSRs) [10], [11]. The calibration deviation caused by the difference in spectral range and RSRs of different sensors can reach up to 10% [12]. The difference in illumination viewing geometry is mainly associated with the bidirectional reflectance distribution function (BRDF) effects [13], which may introduce as much as 15% bias in the cross calibration [14].

To account for the effect of the spectral difference, using radiative transfer equations to estimate the reflectance of the

Manuscript received October 23, 2020; revised February 1, 2021; accepted March 1, 2021. This work was supported in part by the National Key Research and Development Program of China under Grant 2020YFA0608704, in part by the National Natural Science Foundation of China under Grant 42090012 and Grant 41771379, and in part by the Innovative Research Groups of the Hubei Natural Science under Grant 2020CFA003. *(Corresponding author: Tao He.)*

Jun Lu, Tao He, and Yongjun Zhang are with the School of Remote Sensing and Information Engineering, Wuhan University, Wuhan 430079, China (e-mail: junlurs@whu.edu.cn; taohers@whu.edu.cn; zhangyj@whu.edu.cn).

Shunlin Liang is with the Department of Geographical Sciences, University of Maryland at College Park, College Park, MD 20742 USA (e-mail: sliang@umd.edu).

Color versions of one or more figures in this article are available at https://doi.org/10.1109/TGRS.2021.3067672.

Digital Object Identifier 10.1109/TGRS.2021.3067672

target sensor through the observation of a hyperspectral sensor is a good solution [15]. However, due to the discontinuity in spatial and temporal coverages, hyperspectral data in specific scenes are often unavailable. Another way is to use the RSR and ground measured spectral library to estimate the spectral band adjustment factor (SBAF) of the related band through unary linear regression [16], [17]. However, the SBAF may not be suitable for a target sensor that has bands with significant differences in spectral coverages and RSRs [18], [19].

To mitigate the BRDF effect, choosing the image pairs over simultaneous nadir observations (SNOs) has been widely adopted [20], [21]. However, it is not practical to obtain the SNOs for sensors with medium to high spatial resolutions because their swaths are usually small and the orbits do not usually overlap. Another way to eliminate the BRDF effect is to build a model to normalize the directional reflectance differences between the reference sensor and the target data when SNOs are not available. A few methods have been proposed to build the angular normalization model in recent years: 1) obtaining the accurate BRDF characterizations of the calibration site by ground measurements [17], [22]; 2) choosing pseudoinvariant targets and using the multiyear top-of-atmosphere (TOA) reflectance of the reference sensor to build the BRDF model [23], [24]; and 3) using the MODIS BRDF products to estimate BRDF characterizations of the calibration site [25], [26].

Among the three BRDF correction methods, using MODIS BRDF products instead of surface BRDF modeling has been widely used [27]. It has been applied to Landsat-7 ETM+ [12] and Sentinel-2A MSI [26] that are generally considered to be a narrow field of view (FOV) satellite data. In addition, the MODIS BRDF products have been used in the cross calibration of sensors with wide FOV (WFV). For example, Liu *et al*. [28] used the MODIS BRDF products to estimate the BRDF characteristics of the Dunhuang calibration site and simulate the TOA reflectance of Gaofen-1 (GF-1) data, in which the view zenith angle (VZA) can reach to 40° to carry out the cross calibration. Calculating the ratio of the directional reflectance in two illumination viewing geometries using the MODIS BRDF product and using the ratio to estimate the reflectance under the illumination viewing geometry of the target sensor is a good solution [29]. However, due to the coarse spatial resolution of MODIS BRDF product (500 m), the directional reflectance estimation of medium-resolution satellite data (e.g., 30 m) will suffer from the effect of "mixed pixels" [27]. Thus, previous methods based on a simple relationship (e.g., linear ratios) of directional reflectances between two sensors may not work because of the nonlinear relationship when the mixed pixels with mixed BRDFs are included in samples.

Every spaceborne sensor will suffer from the degradation processes during its operational time, one of which is the change in the response of the instrument's radiation measurement [30], [31]. In the case of satellites without on-board calibration capabilities, such as Air Force Satellite-C (FASat-C) [32], Operational Line-scan System of Defense Meteorology Satellite Program (DMSP-OLS) [33], and the WFV on-board the GF-1 satellite launched by China, the degradation of the sensor must be monitored and compensated relying on radiometric calibration. Thus, accurate and frequent calibrations are urgently needed for deriving useful and reliable quantitative information from the satellite data [34].

The Gaofen-4 (GF-4) is China's first high-resolution geostationary optical satellite launched on December 29, 2015. It is equipped with a panchromatic and multispectral sensor (PMS) and a staring optical imager, which has a 50-m spatial resolution in the visible and near-infrared (VNIR) range and 400-m resolution in medium wave infrared [35], and the VZA can reach to 70° [36]. It has the highest resolution among the geostationary orbit satellites in the world [35], [37]. The high spatial resolution and short revisit period enable GF-4 to provide fast, reliable, and stable optical remote sensing data for various applications, such as environmental protection, disaster risk forecasting, and forest fire monitoring, when accurate and timely radiometric calibration can be maintained [38]. However, because of the sensor degradation, radiometric errors could reach 30% [14] without timely calibration activities, particularly during the early period after its launch.

There are several difficulties in the cross calibration of GF-4 data: 1) the spectral characteristics (bandwidth and RSR) of GF-4 PMS are different from those of existing satellite sensors, leading to different reflectance between the GF-4 PMS and other sensors; 2) the viewing geometries of GF-4 is quite different from the polar-orbiting satellite sensors commonly used for cross calibration (e.g., Landsat and MODIS), and therefore, the BRDF effects need to be considered when ray-matched observations are scarcely available; and 3) different from other medium-resolution satellites, GF-4 PMS is a task-based sensor without continuous observations over the same region or with the same repeating cycle, and therefore, traditional methods that require observations over certain calibration sites cannot be applied to such sensors.

To mitigate the effect of differences in the spectral and illumination viewing geometry of GF-4 PMS and reference sensors and, finally, to achieve the near-real-time calibration of GF-4 data, we proposed a data harmonization method, which includes band conversion and BRDF correction to estimate the observation of GF-4 PMS by Landsat-8 OLI. The Landsat-8 OLI has similar spectral bands and spatial resolutions to that of GF-4 PMS in the VNIR spectral range, the data of which are freely available and have a global land coverage. The uncertainty of calibration for OLI is within ±3% [3], and the mean bias of surface reflectance in each band is within 5% [39]. It is suitable for choosing the Landsat-8 OLI data as the reference data to calibrate the GF-4 PMS data.

## II. Data and Methods

### A. Data

The Landsat-8 OLI Collection 1 Level 2 surface reflectance product [40], [41] was collected from the United States Geological Survey (USGS) (https://earthexplorer.usgs.gov/). The basic information about GF-4 PMS and Landsat-8 OLI is listed in Table I. In this study, we have four criteria for the image selection, which includes: 1) the images should include multiple types of land cover (e.g., vegetation, water, and bare soil); 2) the VZA of the images should be within 60°; 3) the

TABLE I
BASIC INFORMATION OF GF-4 PMS AND LANDSAT-8 OLI

| | | GF-4 PMS | Landsat-8 OLI |
|---|---|---|---|
| Band(nm) | blue | 450-520 | 450-510 |
| | green | 520-600 | 530-590 |
| | red | 630-690 | 640-670 |
| | Near-infrared | 760-900 | 850-880 |
| Spatial resolution (m) | | 50 | 30 |
| Swath (km) | | 400 | 185 |
| Quantization (bits) | | 10 | 12 |

acquisition time of the GF-4 should be within five days of the Landsat-8 over the same region; and 4) the overlapping area of the two images should be cloud-free. Based on the image pair composition criteria, we collected a total of 39 image pairs from June to December 2016. We selected two image pairs per month: one for the calculation of calibration coefficient and the other one for the validation. There were 14 image pairs composed of GF-4 and Landsat-8 data used to carry out the calibration and validation. Seven of them were used to calculate calibration coefficients, and the other seven were used for validation. The information of the images used in the calibration and validation is listed in Table II.

The aerosol optical depth (AOD) contained in the MODIS aerosol product (MOD04) [42], [43] from the Terra satellite was used in the radiative transfer simulation of this study. The MODIS aerosol product has a spatial resolution of $10 \times 10$ km, which can be downloaded from the official website of the National Aeronautics and Space Administration (NASA) (https://search.earthdata.nasa.gov/). In this article, we assumed that the MODIS AOD obtained on the same day as the GF-4 data acquisition could be used to represent the aerosol properties of the GF-4 images.

The MODIS BRDF product (MCD43A1) Collection 6 [44] was used to provide the surface BRDF model parameters. The product provides three parameters that are the inputs of the Ross–Li BRDF model [13], [45] to simulate the directional reflectance of certain illumination viewing geometry. The MCD43A1 data are generated by combining the Terra and Aqua data and have an accumulation of 16 days. The spatial resolution is 500 m. The MCD43A1 was obtained from the Level-1 and Atmosphere Archive & Distribution System (LAADS) Distributed Active Archive Center (DAAC) (https://ladsweb.modaps.eosdisnasa.gov/).

The field measurements of surface spectra were taken in June 2016 in Dunhuang to help validate our calibration results, provided by the China Center for Resources Satellite Data and Application (CRESDA), including three surface reflectance spectra of gypsum, desert, and water.

The illumination viewing geometries of GF-4 and Landsat-8 images are plotted in Fig. 1. The angles of the satellite and the sun represent the center pixel of each image. As shown in Fig. 1, the major difference is the VZAs of GF-4 and Landsat-8. The Landsat-8 is considered to be a nadir view satellite, and the VZAs of the images used in the experiment are all within 5.5°. In comparison, the VZAs of the GF-4 images are much larger, and the maximum VZA exceeds 50°. The absolute deviation of the solar azimuth angle (SAA) between GF-4 and Landsat-8 exceeds 60°.

### *B. Cross-Calibration Method of GF-4*

In this article, a radiometric cross-calibration technique for GF-4 PMS with Landsat-8 OLI was used. The surface reflectance of GF-4 PMS was calculated from the Landsat-8 OLI surface reflectance through band conversion and BRDF correction. Then, the TOA reflectance of GF-4 was simulated with the second simulation of the satellite signal in the solar spectrum (6S) radiative transfer model [46]. Finally, the cross calibration of GF-4 was performed. The procedure is illustrated in Fig. 2, and the major steps are discussed below in detail.

*1) Band Conversion:* The differences in observations of two sensors that arise from the different RSRs need to be considered. The bandwidths and RSRs of Landsat-8 OLI and GF-4 PMS are plotted in Fig. 3. The GF-4 PMS has a broader spectral coverage among the four VNIR compared with Landsat-8 OLI and also has a significant difference in RSRs, especially in the blue and NIR bands. Thus, a spectral band conversion should be conducted to mitigate the effects of RSRs differences.

The reflectance for an object in a certain band can be estimated by [14], [29]

$$\rho = \int_a^b f(\lambda)\Gamma(\lambda)d\lambda \Big/ \int_a^b \Gamma(\lambda)d\lambda \tag{1}$$

where $\rho$ is the simulated reflectance of GF-4 PMS and Landsat-8 OLI, $\lambda$ is the wavelength, $\Gamma(\lambda)$ is the RSR, $a$ and $b$ are the spectral ranges of a specific band, and $f(\lambda)$ is the *in situ* measured spectrum. In this article, 245 surface reflectance spectrum samples were collected from the USGS and Advanced Spaceborne Thermal Emission and Reflection Radiometer (ASTER) spectral libraries [47]. These samples included vegetation, soil, rock, water, snow, and ice [48], [49]. The surface spectrum was then used to establish the relationship between PMS and OLI by a multiple linear regression (MLR) model [19], and then, the simulated spectral reflectance of GF-4 PMS by the true Landsat-8 OLI surface reflectance can be obtained

$$\rho'_{\mathrm{PMS}}(j) = \sum_{i=1}^{4} \rho_{\mathrm{OLI}}(i) \cdot C_i \tag{2}$$

where $\rho'_{\mathrm{PMS}}(j)$ is the simulated reflectance of GF-4 in band $j$, $\rho_{\mathrm{OLI}}(i)$ is the true surface reflectance of Landsat-8 in band $i$, and $C_i$ is the SBAFs.

*2) BRDF Correction:* As shown in Fig. 1, the absolute difference in VZAs between GF-4 PMS and Landsat-8 OLI is greater than 45°, and the difference in SAAs is 60°. The angular effect would lead to disparities between the observations of these two sensors. Thus, the reflectance of Landsat-8 OLI cannot represent the true observation of GF-4 PMS directly due to the effect of surface BRDF and the reflectance from different atmospheric paths introduced by the different illumination viewing geometry [29].

In this article, we proposed a general method to implement the BRDF correction with the help of the MODIS BRDF product (MCD43A1). Because GF-4 PMS and Landsat-8 OLI observed the same target with different illumination viewing

TABLE II
BASIC INFORMATION ABOUT THE IMAGES USED IN THE CALIBRATION AND VALIDATION

| | GF-4 PMS | | | | | Landsat-8 OLI | | | | |
|---|---|---|---|---|---|---|---|---|---|---|
| | Date (MM-DD) | UTC* | Longitude** (°) | Latitude** (°) | SZA*** | Date (MM-DD) | UTC* | Longitude** (°) | Latitude** (°) | SZA*** |
| Calibration | 06-16 | 01:51:53 | 89.570 | 42.690 | 32.802 | 06-19 | 04:43:41 | 89.865 | 43.179 | 25.331 |
| | 07-01 | 02:29:20 | 106.081 | 37.905 | 16.635 | 07-01 | 03:30:51 | 107.006 | 38.900 | 24.145 |
| | 08-01 | 04:08:20 | 112.147 | 41.348 | 25.436 | 08-06 | 03:05:07 | 114.583 | 41.755 | 31.564 |
| | 09-04 | 02:03:30 | 104.945 | 40.167 | 44.649 | 09-01 | 03:43:33 | 103.913 | 38.900 | 35.766 |
| | 10-05 | 02:26:23 | 100.939 | 40.503 | 47.671 | 10-10 | 03:49:35 | 102.361 | 38.905 | 47.987 |
| | 11-11 | 03:05:35 | 106.176 | 40.188 | 58.244 | 11-13 | 03:37:30 | 105.443 | 38.900 | 58.471 |
| | 12-01 | 03:44:20 | 100.978 | 40.402 | 60.046 | 12-06 | 03:44:04 | 103.457 | 37.470 | 62.846 |
| Validation | 06-18 | 03:50:20 | 110.439 | 40.922 | 18.348 | 06-15 | 03:30:18 | 107.464 | 40.327 | 23.593 |
| | 07-01 | 02:29:20 | 106.081 | 37.905 | 25.801 | 07-01 | 03:30:27 | 107.453 | 40.328 | 24.937 |
| | 08-01 | 03:59:20 | 115.393 | 31.955 | 15.015 | 08-01 | 02:49:21 | 116.158 | 33.173 | 25.705 |
| | 09-06 | 03:30:20 | 101.048 | 40.401 | 41.257 | 09-06 | 04:01:43 | 99.723 | 40.328 | 38.231 |
| | 10-05 | 02:26:23 | 100.939 | 40.503 | 49.510 | 10-08 | 04:01:32 | 99.721 | 40.333 | 47.917 |
| | 11-15 | 03:01:56 | 106.090 | 40.260 | 58.992 | 11-15 | 03:24:45 | 108.979 | 40.329 | 60.754 |
| | 12-02 | 03:20:32 | 120.379 | 36.774 | 60.367 | 12-07 | 02:48:27 | 117.364 | 37.470 | 62.221 |

*: UTC stands for Coordinated Universal Time; **: Longitude and Latitude are the center longitude and latitude of each image; ***: SZA stands for Solar Zineth Angle;

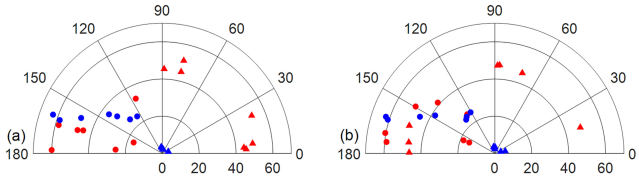


Fig. 1. Illumination viewing geometries of the 14 image pairs used in (a) calibration and (b) validation. The red circles and squares represent the sun and sensor's locations of GF-4 data. The blue circles and squares represent the sun and the sensor's locations of Landsat-8 data. These angles can be obtained from the metadata.

geometries, the MODIS products were used as a bridge to simulate the directional reflectance of GF-4 PMS by the directional reflectance of Landsat-8 OLI.

The reflectances under the two illumination viewing geometries were simulated by MCD43A1 first through the Ross–Li kernel-driven model [50], [51]

$$\begin{cases} R(\theta_s,\theta_v,\varphi) = f_{\text{iso}} + f_{\text{vol}}K_{\text{vol}}(\theta_s,\theta_v,\varphi) \\ \qquad\qquad + f_{\text{geo}}K_{\text{geo}}(\theta_s,\theta_v,\varphi) \\ R'(\theta_s',\theta_v',\varphi') = f_{\text{iso}} + f_{\text{vol}}K_{\text{vol}}(\theta_s',\theta_v',\varphi') \\ \qquad\qquad + f_{\text{geo}}K_{\text{geo}}(\theta_s',\theta_v',\varphi') \end{cases} \tag{3}$$

where $R$ and $R'$ are the directional reflectances of GF-4 PMS and Landsat-8 OLI, $\theta_s, \theta_v$, and $\varphi$ are the solar zenith angle (SZA), VZA, and relative azimuth angle (RAA) of the sensor and the sun of GF-4 PMS, $\theta_s', \theta_v'$, and $\varphi'$ are the SZA, VZA, and RAA of the sensor and the sun of Landsat-8 OLI, $K_{\text{geo}}$ and $K_{\text{vol}}$ are the kernels representing the geometric optical mutual shadowing and volumetric scattering components of the surface reflectance, respectively, $f_{\text{geo}}$ and $f_{\text{vol}}$ are the weights of the two components, and $f_{\text{iso}}$ is the isotropic reflectance component [51]. $f_{\text{geo}}$, $f_{\text{vol}}$, and $f_{\text{iso}}$ are provided by MCD43A1. The simulation of surface reflectance in any specific illumination viewing geometry can be taken through (3) when the SZA, VZA, and RAA are determined.

Then, we established the relationship between $R$ and $R'$. Considering the effect of "mixed pixel", we chose the homogeneous pixels in the $R$ and $R'$ to build the BRDF correction model. The homogeneous pixels were chosen by the coefficient of variation (CV, the ratio of the standard deviation to the mean value). A $15 \times 15$ window was built on the $\rho'_{\text{PMS}}$ based on the selected pixels in $R'$. If the CV of the pixels within the window is less than 1%, the corresponding pixels in the $R$ and $R'$ could be considered a homogeneous pixel pair [16].

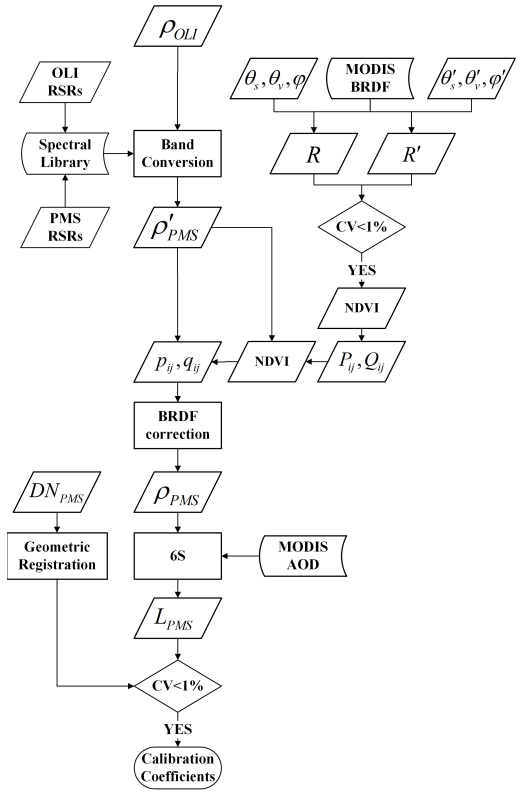


Fig. 2. Workflow of the radiometric cross-calibration method. $\rho_{\text{OLI}}$ is the surface reflectance of Landsat-8 OLI, RSR represents the normalized RSR, $\rho'_{\text{PMS}}$ is the simulated spectral reflectance of GF-4 PMS, NDVI represents the normalized difference vegetation index, CV represents the coefficient of variation, $\theta_s, \theta_v, \varphi$ and $\theta_s', \theta_v', \varphi'$ are the SZAs, VZAs, and RAAs of the GF-4 PMS and Landsat-8 OLI images, $R$ and $R'$ are the simulated directional reflectances under the illumination viewing geometries of GF-4 PMS and Landsat-8 OLI, $P_{ij}$, $Q_{ij}$ and $p_{ij}$, $q_{ij}$ are the BRDF correction coefficients, $\rho_{\text{PMS}}$ and $L_{\text{PMS}}$ are the surface directional reflectance and the TOA radiance of GF-4 PMS, respectively, and DN represents the digital number.

Because of the nonlinear relationship between the directional reflectances under different viewing geometries of GF-4 PMS and Landsat-8 OLI, we built a piecewise linear model to calculate the BRDF correction coefficient between $R$ and $R'$. An assumption was made that the same land

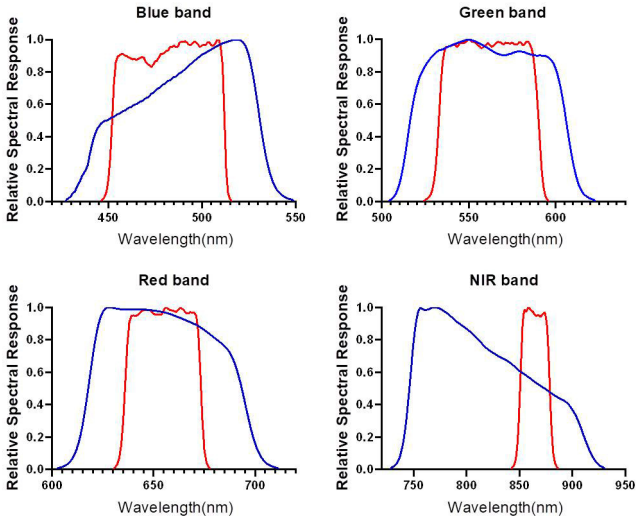


Fig. 3. RSRs for the corresponding bands in the GF-4 and Landsat-8. The blue plots represent GF-4 PMS RSRs; the red plots represent Landsat-8 OLI RSRs. The blue, green, red, and NIR bands correspond to bands 2, 3, 4, and 5 of GF-4 PMS and Landsat-8 OLI, respectively.

cover type has the same BRDF shape, but the magnitude of reflectance may vary [52]–[54]. The normalized difference vegetation index (NDVI) was used as an index to distinguish different land cover types (e.g., bare soils, vegetation, snow/ice, and water). For the same land cover type, variations in BRDF shape throughout a year are limited and linked to the NDVI [55], [56]. The homogeneous pixels were divided into several classes with an interval of 0.2 (>0, 0–0.2, 0.2–0.4, 0.4–0.6, and 0.6<) based on NDVI [54]. Then, a linear model was built on each class for each band in $R$ and $R'$, as shown in (4). Equation (5) shows a combined set of regression coefficients for all the NDVI intervals for a spectral band

$$R_{ij} = R'_{ij} \cdot P_{ij} + Q_{ij} \tag{4}$$

$$P = P_1 \cup P_2 \cup P_3 \cdots \cup P_i; \quad Q = Q_1 \cup Q_2 \cup Q_3 \cdots \cup Q_i \tag{5}$$

where $P$ and $Q$ are BRDF correction coefficients, $i$ is the class index, and $j$ is the band index. After the linear models of all classes were built, the piecewise linear BRDF correction model for a spectral band in a scene can be obtained.

In order to apply the BRDF correction coefficients derived by $R$ and $R'$ to $\rho'_{\mathrm{PMS}}$, we assumed that the BRDF shape is dependent on land cover type and independent of the spatial resolution [27]. Then, we calculated the NDVI of $\rho'_{\mathrm{PMS}}$ and divided it into several classes with an interval of 0.2. We applied $P$ and $Q$ to the same class in each band derived by $\rho'_{\mathrm{PMS}}$

$$p_{ij} = P_{ij}; q_{ij} = Q_{ij} \tag{6}$$

where $p$ and $q$ are the BRDF correction coefficients for GF-4 PMS. Therefore, the directional reflectance under the illumination viewing geometry of GF-4 PMS can be simulated by $\rho'_{\mathrm{PMS}}$ through

$$\rho_{\mathrm{PMS}}(i,j) = \rho'_{\mathrm{PMS}}(i,j) \cdot p_{ij} + q_{ij} \tag{7}$$

where $\rho_{\mathrm{PMS}}$ is the simulated 30-m surface directional reflectance under the illumination viewing geometry of GF-4 PMS by $\rho'_{\mathrm{PMS}}$.

*3) Calculation of Calibration Coefficients:* After the estimation of surface reflectance at a specific spectral band under the illumination viewing geometry of GF-4 PMS by Landsat-8 OLI surface reflectance, we used the 6S to obtain the TOA radiance of GF-4 PMS by the forward simulation model. The TOA reflectance can be obtained by [46]

$$\rho^{\mathrm{TOA}}_{\mathrm{PMS}}(\theta_s,\theta_v,\varphi) = \rho_a(\theta_s,\theta_v,\varphi) + \frac{T(\theta_s)T(\theta_v)\rho_{\mathrm{PMS}}(\theta_s,\theta_v,\varphi)}{1 - S\rho_{\mathrm{PMS}}(\theta_s,\theta_v,\varphi)} \tag{8}$$

where $\rho^{\mathrm{TOA}}_{\mathrm{PMS}}$ is TOA reflectance of GF-4, $\rho_a$ is the atmospheric path reflectance, $S$ is the spherical albedo of the atmosphere, and $T(\theta_s)$ and $T(\theta_v)$ are the total downward and upward transmittances, respectively. Then, $\rho^{\mathrm{PMS}}_{\mathrm{TOA}}$ was converted to TOA radiance by

$$L_{\mathrm{PMS}} = \frac{\rho^{\mathrm{TOA}}_{\mathrm{PMS}} \mathrm{ESUN}_{\mathrm{PMS}} \cos(\theta_s)}{\pi d^2} \tag{9}$$

where $L_{\mathrm{PMS}}$ is the TOA radiance, $d$ is the Earth–Sun distance, and $\mathrm{ESUN}_{\mathrm{PMS}}$ is the solar spectral radiance at the TOA of GF-4 PMS, which is published by CRESDA. Finally, $L_{\mathrm{PMS}}$ and the digital number (DN) value of GF-4 PMS were used to calculate the calibration coefficients through a linear calibration model

$$L_{\mathrm{PMS}} = \mathrm{gains} \cdot DN_{\mathrm{PMS}} + \mathrm{offset} \tag{10}$$

where $\mathrm{DN}_{\mathrm{PMS}}$ is the DN value of GF-4 PMS, and gains and offset are the calibration coefficients. To mitigate the mismatching of the footprints of $L_{\mathrm{PMS}}$ and $\mathrm{DN}_{\mathrm{PMS}}$, we carried out a geometric registration between those two data. Similarly, we chose the homogeneous pixel to build the linear calibration model. Based on $L_{\mathrm{PMS}}$ (30 m) and $\mathrm{DN}_{\mathrm{PMS}}$ (50 m), $5 \times 5$ and $3 \times 3$ windows were built on the corresponding pixel, respectively. When the CVs of the pixels in the two windows are all less than 1%, the center pixel of the two windows can be chosen for building the calibration model.

### C. Validation of Calibration Coefficients

The evaluation of calibration accuracy is performed in two ways. The first method is based on the image. In the validation image pair, $\mathrm{DN}_{\mathrm{PMS}}$ was converted to the calculated TOA reflectance, and $\rho^{\mathrm{PMS}}_{\mathrm{TOA}}$ can be simulated by Landsat-8 OLI through band conversion and BRDF correction. The second method is based on the *in situ* measurements at the Dunhuang calibration site conducted by the CRESDA in June 2016. The *in situ* surface spectrum was converted to PMS equivalent surface reflectance at a specific band by (1), and then, the TOA reflectance calculated by the *in situ* measurement can be obtained through 6S radiative transfer. We derived $\rho^{\mathrm{PMS}}_{\mathrm{TOA}}$ of the calibration site by the calibration coefficients through the method proposed in this article and the official released, respectively. A comparison of the two different reflectances with the *in situ* simulated TOA reflectance was implemented at last. The radiometric calibration accuracy can be quantified by

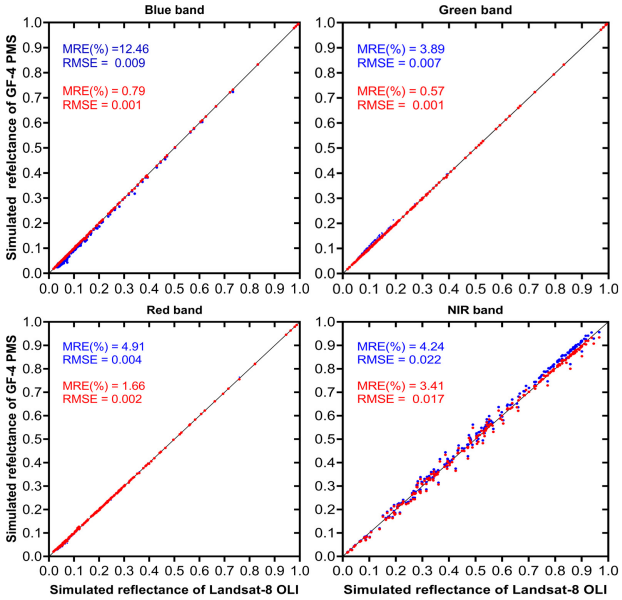


Fig. 4. Band conversion results. The $x$-axis is the simulated reflectance of Landsat-8 OLI, and the $y$-axis is the simulated reflectance of GF-4 PMS using the surface spectra and sensors' normalized RSR data. The blue points represent the simulated reflectance pair of GF-4 PMS and Landsat-8 OLI without band conversion. The red points are the simulated reflectance pair after band conversion.

TABLE III
SBAFs OF LANDSAT-8 OLI AND GF-4 PMS

| | | Landsat-8 | | | | |
|---|---|---|---|---|---|---|
| | | Band2 | Band3 | Band4 | Band5 | Intercept |
| GF-4 | Band2 | 0.8651 | 0.1675 | -0.0324 | | 0.0001 |
| | band3 | 0.0812 | 0.8530 | 0.0679 | | -0.0003 |
| | band4 | | 0.0402 | 0.9565 | | 0.0027 |
| | band5 | | | | 0.9773 | -0.0006 |

mean relative error (MRE) and root mean square error (RMSE)

$$\mathrm{MRE}(\%) = \frac{100\%}{n}\sum_{i=1}^{n}\frac{\left|\rho_{\mathrm{TOA},i}^{\mathrm{calculated}} - \rho_{\mathrm{TOA},i}^{\mathrm{PMS}}\right|}{\rho_{\mathrm{TOA},i}^{\mathrm{PMS}}} \tag{11}$$

$$\mathrm{RMSE} = \sqrt{\frac{\sum_{i=1}^{n}\left(\rho_{\mathrm{TOA},i}^{\mathrm{PMS}} - \rho_{\mathrm{TOA},i}^{\mathrm{calculated}}\right)^2}{n}} \tag{12}$$

where $\rho_{\mathrm{TOA}}^{\mathrm{calculated}}$ is the TOA reflectance calculated by the calibration coefficients, $\rho_{\mathrm{TOA}}^{\mathrm{PMS}}$ is the TOA reflectance simulated by the proposed method, and $n$ is the number of samples.

## III. Results and Discussion

### A. Band Conversion Results

Fig. 4 plots the surface reflectances of GF-4 PMS and Landsat-8 OLI simulated by *in situ* spectrum and RSRs. The results suggested that the simulated reflectance closely matches the PMS reflectance after band conversion, especially for the blue band. The SBAFs of GF-4 PMS and Landsat-8 OLI were obtained by fitting the simulated reflectance data through MLR analysis, and the SBAFs are shown in Table III. These SBAFs illustrate the necessity of using the MLR to estimate the reflectance of GF-4 instead of calculating the scale factor of each band separately.

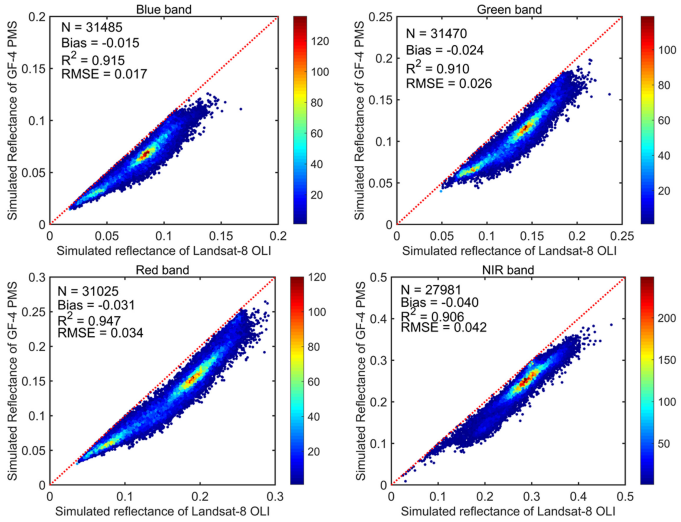


Fig. 5. Directional reflectances simulated by MCD43A1 under the illumination viewing geometries of GF-4 PMS and Landsat-8 OLI. The $x$-axis represents the reflectance under the illumination viewing geometry of Landsat-8 OLI, and the $y$-axis represents the reflectance under the illumination viewing geometry of GF-4 PMS. The red line is the 1:1 line.

### B. BRDF Correction Coefficients

The directional reflectances simulated by MCD43A1 under the illumination viewing geometries of GF-4 PMS and Landsat-8 OLI were plotted in Fig. 5. There is a nonlinear distribution of reflectance in the two illumination viewing geometries, especially in the visible bands.

Using the piecewise linear fitting method, the directional reflectance under the illumination viewing geometry of GF-4 PMS can be estimated. For illustration, we took an image pair consisted of GF-4 and near-concurrent Landsat-8. The GF-4 data obtained on June 16, 2016, and the Landsat-8 data obtained on June 19, 2016. The BRDF correction coefficients of the directional reflectance under the two illumination viewing geometries of the homogeneous pixels among the five different land cover types are listed in Table IV. Classes 1–5 represent five different land cover types approximated with an interval of 0.2 in NDVI. $N$ is the number of homogeneous pixels, and $P$ and $Q$ are the parameters of the linear model in (4).

Most of the $R^2$ values are above 0.9 except for class 2 (NDVI $\in$ (0.2, 0.4]) in the green and NIR bands and class 5 (NDVI $>$ 0.6) in the NIR band. The slope of the fit line of the five classes in each band shows a significant difference. The slope of the blue band ranges from 0.869 to 0.936, and the CV of the slope is 2.78%. The slope of the green band ranges from 0.835 to 0.928, and the CV of the slope is 3.75%. The slope of the red band ranges from 0.829 to 0.941, and the CV of the slope is 4.97%. The slope of the NIR band ranges from 1.080 to 1.178, and the CV of the slope is 3.74%. There is a certain nonlinear feature of the reflectance in the two illumination viewing geometries according to the distribution of the reflectance of all samples. This means that using simple linear models to carry out the BRDF correction in certain illumination viewing geometry may result in some errors.

TABLE IV
BRDF CORRECTION COEFFICIENTS OF GF-4 PMS DATA OBTAINED ON JUNE 16, 2016

| Band ($j$) | Class ($i$) | $N$ | $P$ | $Q$ | $R^2$ |
|---|---|---|---|---|---|
| Blue band | 1 | 886 | 0.887** | 0.009** | 0.943** |
| | 2 | 326 | 0.870* | -0.003* | 0.904* |
| | 3 | 291 | 0.888** | -0.001** | 0.955** |
| | 4 | 246 | 0.936** | -0.003** | 0.971** |
| | 5 | 135 | 0.894** | 0.000** | 0.964** |
| Green band | 1 | 624 | 0.892** | 0.006** | 0.904** |
| | 2 | 567 | 0.835* | -0.004* | 0.898* |
| | 3 | 348 | 0.886** | -0.006** | 0.948** |
| | 4 | 242 | 0.928** | -0.009** | 0.965** |
| | 5 | 124 | 0.883** | -0.004** | 0.953** |
| Red band | 1 | 770 | 0.941** | 0.000** | 0.952** |
| | 2 | 523 | 0.829* | -0.002* | 0.909* |
| | 3 | 402 | 0.857** | 0.001** | 0.951** |
| | 4 | 237 | 0.905*** | -0.003*** | 0.973*** |
| | 5 | 103 | 0.867*** | 0.001*** | 0.963*** |
| NIR band | 1 | 699 | 1.080*** | -0.003*** | 0.972*** |
| | 2 | 598 | 1.178* | -0.046* | 0.876* |
| | 3 | 405 | 1.120** | -0.019** | 0.930** |
| | 4 | 285 | 1.086** | -0.006** | 0.923** |
| | 5 | 199 | 1.084* | 0.000* | 0.884* |

*, **, *** : The confidence interval of 90%, 95%, and 99%.

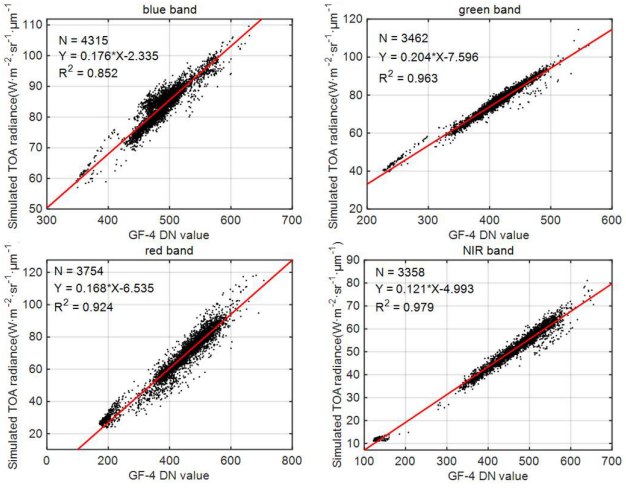


Fig. 6. Simulated TOA radiance with GF-4 spectral bands and viewing geometries against GF-4 PMS DN values. Linear fits resulted in cross-calibration coefficients. The GF-4 data were obtained on June 16, 2016, the acquisition time of Landsat-8 was June 19, 2016, and the path/raw is 141/30. The red line is the fitting curve.

### C. Calibration and Validation Results

Based on the normalized Landsat-8 OLI reflectance with the spectral bands and illumination viewing geometry of GF-4 PMS, we calculated the corresponding TOA radiance by (9). To eliminate mismatches of the footprints of Landsat-8 OLI and GF-4 PMS, we used the homogeneous pixel to build the calibration model. An example of the linear calibration model is shown in Fig. 6.

The calibration results show that the calibration models have high accuracy. $R^2$ exceeds 0.85 for all four bands. However, $R^2$ for the blue band is slightly lower than the rest bands, which is likely caused by the uncertainty of the AOD estimation because the impact of aerosols tends to be stronger in the shorter wavelength [40], [57]. There is a difference in overpass times of MODIS and GF-4 PMS. Thus, the MODIS aerosol products may not represent the atmospheric condition at the overpass time of the GF-4 PMS image accurately due to the diurnal variation of AOD.

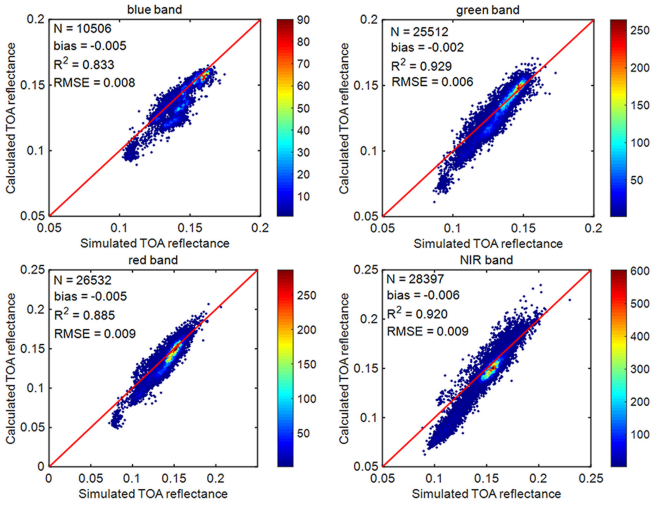


Fig. 7. Validation of calibrated TOA reflectance of GF-4 using simulated TOA reflectance from nonsimultaneous Landsat-8 data. The GF-4 data were obtained on June 18, 2016, the acquisition time of Landsat-8 was June 15, 2016, and the path/raw is 129/32. The red line is the 1:1 line.

Correspondingly, another GF-4 PMS image obtained on June 18, 2016, was used for validation. The simulated TOA reflectance at a specific spectral band under the illumination viewing geometry of GF-4 PMS through Landsat-8 OLI was obtained by the data normalization method and radiative transfer model. The calculated TOA reflectance was obtained using the DN value of GF-4 PMS. We chose the homogeneous pixels of the calculated TOA reflectance and simulated TOA reflectance of the different bands via the homogeneous pixels selection method. As shown in Fig. 7 the calibration coefficients have a high calibration accuracy of the four bands. The mean bias of each band is $-0.45\%$, and the mean RMSE of the four bands is 0.008.

In order to compare the difference between the calibration coefficients obtained in this article and the official release, we calculated the TOA reflectance of the GF-4 PMS image obtained on June 18, 2016, by the calibration coefficient obtained in this article and the official release, respectively. The MREs of TOA reflectance of red and NIR bands are shown in Fig. 8. The relative difference of TOA reflectance in the red band is concentrated in 7%–10%, and the relative difference in the NIR band is concentrated in 2%–12%. This means that the difference between calibration coefficients is significant, and there is great uncertainty in the calculation of the TOA reflectance using different calibration coefficients.

In addition, the field survey spectrum collected in June 2016 was used to evaluate the accuracy of calibration coefficients obtained from this article and the official release. The result is shown in Fig. 9. The TOA reflectance calculated by the coefficients obtained shows a more favorable agreement than the official release coefficients with the *in situ* simulated TOA reflectance. The validation using ground measurements shows that our calibration results have an improvement of around 14.8% compared with the official released calibration coefficients.

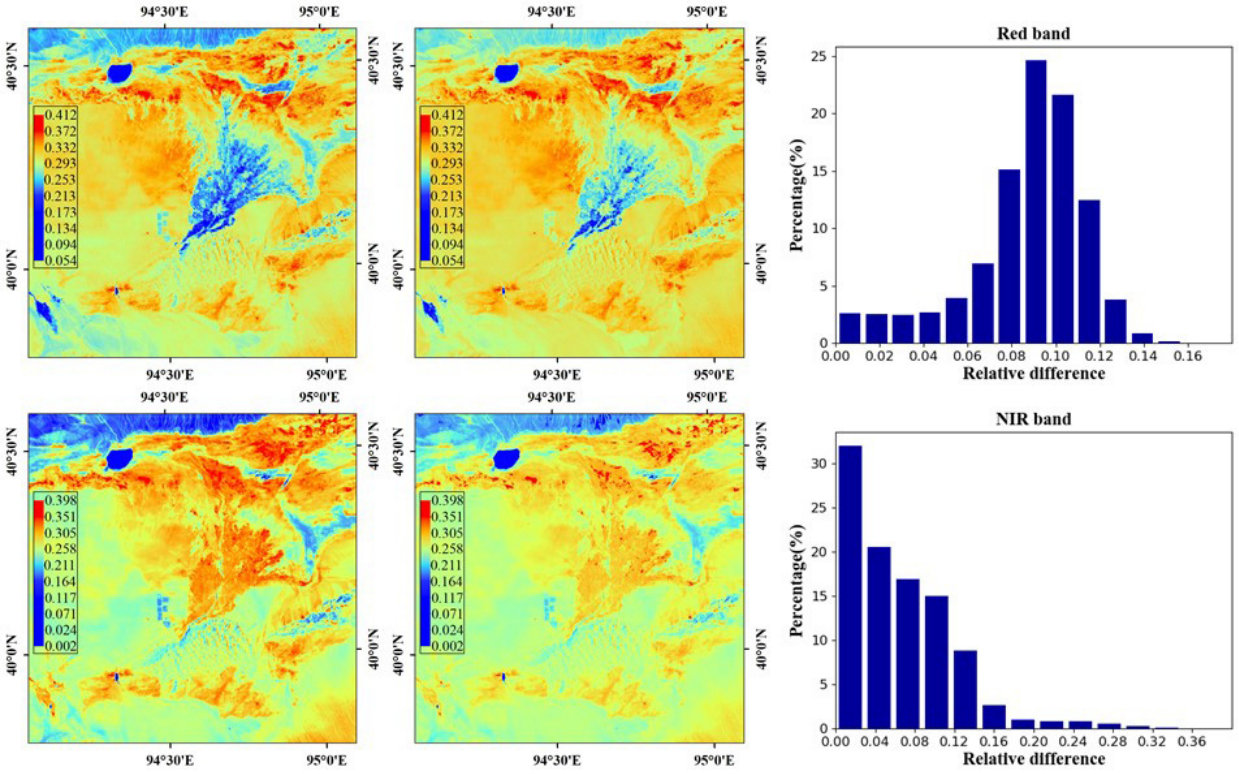


Fig. 8. Comparison of red and NIR band TOA reflectances calculated by the calibration coefficients provided in this article and the CRESDA. The GF-4 PMS data obtained on June 18, 2016. The first row is the TOA reflectance of the red band, and the second row is the NIR band. The first column is the TOA reflectance calculated by the calibration coefficients provided in this article, and the second column is the TOA reflectance calculated by the officially released calibration coefficients. The third column is the relative difference (the absolute value of the difference in the two reflectances divided by the reflectance calculated by the official released calibration coefficients) of the two TOA reflectances.

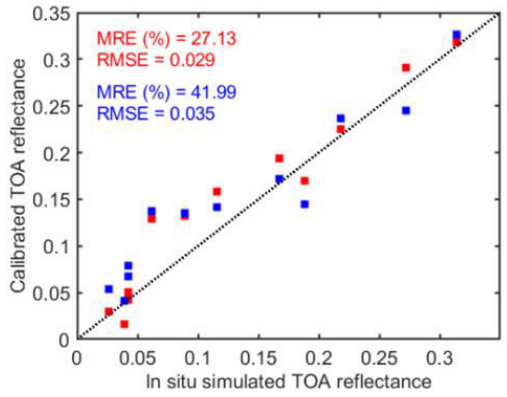


Fig. 9. Validations of the calibrated TOA reflectance of GF-4 using *in situ* simulated TOA reflectance and calibrated TOA reflectance. The blue squares are the TOA reflectance values calculated with the official calibration coefficients. The red squares are the TOA reflectance values calculated with the calibration coefficients obtained by the proposed method in this article. The black dotted line is the 1:1 line.

### *D. Temporal Analysis of the Calibration Coefficients*

In order to capture the degradation of the GF-4 PMS in-orbit, we applied the same data normalization and the cross-calibration method to the other six image pairs obtained in 2016, and a set of calibration coefficients of the time series were determined. The results are listed in Table V.

The $R^2$ values of the four bands in all periods exceed 0.82. This means that the cross calibration that we proposed is stable and reliable. However, the modeling performance of the blue band is relatively poor compared with other bands, and the average $R^2$ value of the blue band is less than 7.9% that of the red band. We also used the other image pairs in all seven periods together and validated the calibration accuracy. The results are shown in Table VI.

The validation results show a high calibration accuracy of the four bands. The MRE of each band of cross calibration is less than 6.65%. In some periods, the RMSE exceeds 1%, but the magnitude is not large. However, there remains a slight underestimation in the blue band, but the error is tolerable. This is possible because of the nonsimultaneous AOD for the retrieval of the MODIS observation. Overall, the method proposed in this article achieves good results in the calibration of the GF-4 PMS with a significant difference in the spectral character and illumination viewing geometry of the Landsat-8 OLI.

In general, the results show degradation of GF-4 PMS. In light of the linear calibration model, the greater the slope, the greater the degradation of the sensor. From June 18 to December 1, 2016, the gains of the blue band increased from 0.176 to 0.297, the gains of the green band increased from 0.207 to 0.263, the gains of the red band increased from 0.165 to 0.241, and the gains of the NIR band increased from 0.121 to 0.185. The fluctuation captured by the temporal calibration according to the variation of the gains may be caused by the unstable performance of the GF-4 PMS in the early time after it was launched.

TABLE V
CALIBRATION COEFFICIENTS FOR GF-4 AT DIFFERENT PERIODS

| | | 2016-06-16 | 2016-07-01 | 2016-08-01 | 2016-09-04 | 2016-10-05 | 2016-11-11 | 2016-12-01 |
|---|---|---|---|---|---|---|---|---|
| Blue band | $gains$ | 0.176 | 0.167 | 0.193 | 0.205 | 0.223 | 0.329 | 0.297 |
| | $offest$ | -2.335 | -11.769 | -16.432 | -9.076 | -15.426 | -39.472 | -10.387 |
| | $R^2$ | 0.852 | 0.828 | 0.922 | 0.894 | 0.939 | 0.864 | 0.821 |
| Green band | $gains$ | 0.204 | 0.188 | 0.289 | 0.237 | 0.240 | 0.304 | 0.263 |
| | $offest$ | -7.596 | -30.334 | -41.823 | -15.039 | -15.409 | -17.283 | -0.025 |
| | $R^2$ | 0.963 | 0.903 | 0.956 | 0.863 | 0.977 | 0.881 | 0.973 |
| Red band | $gains$ | 0.168 | 0.168 | 0.210 | 0.198 | 0.201 | 0.271 | 0.241 |
| | $offest$ | -6.535 | -28.419 | -30.844 | -12.391 | -15.782 | -19.165 | -3.856 |
| | $R^2$ | 0.924 | 0.911 | 0.901 | 0.963 | 0.974 | 0.926 | 0.920 |
| NIR band | $gains$ | 0.121 | 0.124 | 0.153 | 0.170 | 0.130 | 0.200 | 0.185 |
| | $offest$ | -4.993 | -25.515 | -27.644 | -22.996 | -5.422 | -13.659 | -8.658 |
| | $R^2$ | 0.979 | 0.837 | 0.908 | 0.983 | 0.963 | 0.871 | 0.925 |

TABLE VI
EVALUATION OF CALIBRATED TOA REFLECTANCE OF GF-4 USING SIMULATED TOA REFLECTANCE FROM CONCURRENT LANDSAT-8

| | | 2016-06-18 | 2016-07-01 | 2016-08-01 | 2016-09-06 | 2016-10-05 | 2016-11-15 | 2016-12-02 |
|---|---|---|---|---|---|---|---|---|
| Blue band | $N^*$ | 10506 | 11476 | 12907 | 12267 | 11871 | 13133 | 11591 |
| | $MRE(\%)$ | 2.15 | 1.18 | 2.55 | 3.20 | 2.81 | 2.97 | 2.86 |
| | $RMSE$ | 0.008 | 0.007 | 0.008 | 0.010 | 0.005 | 0.009 | 0.008 |
| Green band | $N^*$ | 25512 | 10040 | 12723 | 10126 | 7557 | 15604 | 10309 |
| | $MRE(\%)$ | 3.81 | 2.54 | 4.78 | 2.97 | 2.13 | 3.59 | 2.15 |
| | $RMSE$ | 0.006 | 0.009 | 0.009 | 0.008 | 0.006 | 0.010 | 0.008 |
| Red band | $N^*$ | 26532 | 13170 | 10118 | 10390 | 2024 | 13328 | 9751 |
| | $MRE(\%)$ | 1.20 | 1.14 | 2.26 | 3.27 | 2.46 | 2.93 | 3.16 |
| | $RMSE$ | 0.009 | 0.010 | 0.010 | 0.009 | 0.010 | 0.009 | 0.010 |
| NIR band | $N^*$ | 28397 | 7136 | 10269 | 5415 | 2002 | 5348 | 8607 |
| | $MRE(\%)$ | 2.13 | 3.83 | 6.65 | 4.59 | 2.73 | 6.62 | 3.36 |
| | $RMSE$ | 0.010 | 0.010 | 0.009 | 0.010 | 0.006 | 0.011 | 0.010 |

*: The number of samples.

## IV. CONCLUSION AND DISCUSSION

This article proposes a novel cross-calibration method for medium-resolution multispectral data with a large view angle. The main contributions of this article are as follows: 1) the general data normalization approach can be easily adapted and applied to other optical sensors as long as a suitable reference data set is available and 2) the cross-calibration method does not need actively monitored fixed calibration site and does not rely on ray-matching or coincident matched data, which requires ancillary information to prescribe the atmospheric and surface conditions, including aerosol loadings, surface BRDFs, and a land cover map.

In order to mitigate the difference in spectral coverage and illumination viewing geometry of different sensors, an MLR and piecewise linear model are used to normalize the observations of the different sensors. Choosing the best matching spectrum based on the spectral reflectance of the reference sensor has been widely applied to the implementation of the spectral band conversion between the reference sensor and the uncalibrated sensor [16], [29], [36]. However, due to the small number of the spectrum and the similarity between the *in situ* spectrum of the ground features, the SBAFs obtained by previous methods may unstable.

Our method established the relationship of the two-directional reflectances directly and did not use the reflectance under the nadir view as an intermediate variable [16], [29]. In addition, two directional reflectances with huge difference in the illumination viewing geometry may have an obvious nonlinear distribution when directional reflectances from different land covers were put together (see Fig. 5). This article used a piecewise linear method to establish the relationship between the directional reflectances under two illumination viewing geometries, which avoided the error caused by a single linear model.

The VZAs of the GF-4 PMS images used in this article can exceed 50°. However, the VZA of MODIS is within ±55°. The VZAs of GF-4 at middle and high latitude regions are larger than MODIS. Thus, using the MODIS BRDF parameter to estimate the directional reflectance of GF-4 PMS in middle and high latitude regions may have uncertainty.

This study chooses the homogeneous pixels to calculate the BRDF correction coefficients, which can mitigate the error caused by a significant difference in the spatial resolution of Landsat-8 OLI and MODIS. The homogeneous pixels are chosen based on the CV of the pixels in the moving window. However, there are various criteria for the selection of homogeneous pixels, such as the absolute deviation [57], which is not compared in this study. Besides, the piecewise linear fitting is implemented depending on the NDVI under the assumption that the absolute deviation NDVI of the same ground type was within 0.2. However, if the land use and cover map of the calibration site are available, then the BRDF correction coefficients of different ground types can be fixed using a lookup map [54], [58].

The saturation of the images will affect the stability of the calibration gains [59]. The small variation in calibration gains of each month (see Table V) may be caused by the situation of GF-4 PMS for the unstable performance of the sensor in the early time after it was launched. To obtain stable calibration coefficients, the saturated pixels cannot be used in the calibration modeling [16]. Therefore, the GF-4 PMS image that was largely affected by the saturation problem cannot be used as a candidate image.

The calibration method proposed in this article achieves high-frequency radiometric calibration of GF-4 PMS through Landsat-8 OLI. However, there are still differences in overpass time for the reference sensor and the target sensor. The MODIS aerosol products may introduce errors due to the diurnal variation of AOD. There is a difference in overpass times of MODIS and GF-4 PMS. Thus, the MODIS aerosol products may not represent the atmospheric condition at the overpass time of the GF-4 PMS image accurately. Besides, the longest time interval of the image pair used in the calibration and validation is five days (see Table II); thus, the surface reflectance in the overleap region may have variations during the time interval. Achieving the near-real-time calibration through short revisit cycle data (e.g., MODIS) will be the focus of future research.

## ACKNOWLEDGMENT

The authors would like to thank the United States Geological Survey (USGS) (http://landsat.usgs.gov) for providing Landsat data and the spectral library, the Moderate Resolution Imaging Spectroradiometer (MODIS) Land Team for providing the aerosol and BRDF products (http://earthdata.nasa.gov), and the China Center for Resources Satellite Data and Application (CRESDA) (http://www.cresda.com) for providing GF-4 data and *in situ* spectral measurements.

## REFERENCES

[1] G. Chander, B. L. Markham, and D. L. Helder, "Summary of current radiometric calibration coefficients for landsat MSS, TM, ETM+, and EO-1 ALI sensors," *Remote Sens. Environ.*, vol. 113, no. 5, pp. 893–903, May 2009.

[2] G. Chander, D. L. Helder, D. Aaron, N. Mishra, and A. K. Shrestha, "Assessment of spectral, misregistration, and spatial uncertainties inherent in the cross-calibration study," *IEEE Trans. Geosci. Remote Sens.*, vol. 51, no. 3, pp. 1282–1296, Mar. 2013.

[3] J. Czapla-Myers *et al.*, "The ground-based absolute radiometric calibration of landsat 8 OLI," *Remote Sens.*, vol. 7, no. 1, pp. 600–626, Jan. 2015.

[4] H. Gao, X. Gu, T. Yu, Y. Sun, and Q. Liu, "Cross-calibration of GF-1 PMS sensor with landsat 8 OLI and Terra MODIS," *IEEE Trans. Geosci. Remote Sens.*, vol. 54, no. 8, pp. 4847–4854, Aug. 2016.

[5] K. Obata, T. Miura, H. Yoshioka, A. Huete, and M. Vargas, "Spectral cross-calibration of VIIRS enhanced vegetation index with MODIS: A case study using year-long global data," *Remote Sens.*, vol. 8, no. 1, p. 34, Jan. 2016.

[6] C. Gao, X. Jiang, X. Li, and X. Li, "The cross-calibration of CBERS-02B/CCD visible-near infrared channels with Terra/MODIS channels," *Int. J. Remote Sens.*, vol. 34, nos. 9–10, pp. 3688–3698, May 2013.

[7] A. Angal, X. Xiong, A. Wu, G. Chander, and T. Choi, "Multitemporal cross-calibration of the Terra MODIS and landsat 7 ETM+ reflective solar bands," *IEEE Trans. Geosci. Remote Sens.*, vol. 51, no. 4, pp. 1870–1882, Apr. 2013.

[8] M. M. Farhad, M. Kaewmanee, L. Leigh, and D. Helder, "Radiometric cross calibration and validation using 4 angle BRDF model between landsat 8 and sentinel 2A," *Remote Sens.*, vol. 12, no. 5, p. 806, Mar. 2020.

[9] J. Gorroño, A. C. Banks, N. P. Fox, and C. Underwood, "Radiometric inter-sensor cross-calibration uncertainty using a traceable high accuracy reference hyperspectral imager," *ISPRS J. Photogramm. Remote Sens.*, vol. 130, pp. 393–417, Aug. 2017.

[10] P. M. Teillet, J. L. Barker, B. L. Markham, R. R. Irish, G. Fedosejevs, and J. C. Storey, "Radiometric cross-calibration of the landsat-7 ETM+ and landsat-5 TM sensors based on tandem data sets," *Remote Sens. Environ.*, vol. 78, nos. 1–2, pp. 39–54, Oct. 2001.

[11] P. M. Teillet, G. Fedosejevs, K. J. Thome, and J. L. Barker, "Impacts of spectral band difference effects on radiometric cross-calibration between satellite sensors in the solar-reflective spectral domain," *Remote Sens. Environ.*, vol. 110, no. 3, pp. 393–409, Oct. 2007.

[12] N. Mishra, M. Haque, L. Leigh, D. Aaron, D. Helder, and B. Markham, "Radiometric cross calibration of landsat 8 operational land imager (OLI) and landsat 7 enhanced thematic mapper plus (ETM+)," *Remote Sens.*, vol. 6, no. 12, pp. 12619–12638, Dec. 2014.

[13] W. Lucht, C. B. Schaaf, and A. H. Strahler, "An algorithm for the retrieval of albedo from space using semiempirical BRDF models," *IEEE Trans. Geosci. Remote Sens.*, vol. 38, no. 2, pp. 977–998, Mar. 2000.

[14] A. Yang, B. Zhong, S. Wu, and Q. Liu, "Radiometric cross-calibration of GF-4 in multispectral bands," *Remote Sens.*, vol. 9, no. 3, p. 232, Mar. 2017.

[15] M. Claverie *et al.*, "The harmonized landsat and Sentinel-2 surface reflectance data set," *Remote Sens. Environ.*, vol. 219, pp. 145–161, Dec. 2018.

[16] J. Li, L. Feng, X. Pang, W. Gong, and X. Zhao, "Radiometric cross calibration of Gaofen-1 WFV cameras using Landsat-8 OLI images: A simple image-based method," *Remote Sens.*, vol. 8, no. 5, p. 411, May 2016.

[17] B. Zhong, A. Yang, S. Wu, J. Li, S. Liu, and Q. Liu, "Cross-calibration of reflective bands of major moderate resolution remotely sensed data," *Remote Sens. Environ.*, vol. 204, pp. 412–423, Jan. 2018.

[18] T. He, S. Liang, D. Wang, X. Chen, D.-X. Song, and B. Jiang, "Land surface albedo estimation from Chinese HJ satellite data based on the direct estimation approach," *Remote Sens.*, vol. 7, no. 5, pp. 5495–5510, May 2015.

[19] T. He *et al.*, "Evaluating land surface albedo estimation from landsat MSS, TM, ETM+, and OLI data based on the unified direct estimation approach," *Remote Sens. Environ.*, vol. 204, pp. 181–196, Jan. 2018.

[20] J. Gil, J. F. Rodrigo, P. Salvador, D. Gómez, J. Sanz, and J. L. Casanova, "An empirical radiometric intercomparison methodology based on global simultaneous nadir overpasses applied to landsat 8 and Sentinel-2," *Remote Sens.*, vol. 12, no. 17, p. 2736, Aug. 2020.

[21] A. Angal, X. Xiong, and A. Wu, "Monitoring the on-orbit calibration of Terra MODIS reflective solar bands using simultaneous Terra MISR observations," *IEEE Trans. Geosci. Remote Sens.*, vol. 55, no. 3, pp. 1648–1659, Mar. 2017.

[22] B. Zhong, Y. Zhang, T. Du, A. Yang, W. Lv, and Q. Liu, "Cross-calibration of HJ-1/CCD over a desert site using Landsat ETM + imagery and ASTER GDEM product," *IEEE Trans. Geosci. Remote Sens.*, vol. 52, no. 11, pp. 7247–7263, Nov. 2014.

[23] S. Uprety and C. Cao, "Suomi NPP VIIRS reflective solar band on-orbit radiometric stability and accuracy assessment using desert and Antarctica Dome C sites," *Remote Sens. Environ.*, vol. 166, pp. 106–115, Sep. 2015.

[24] E. F. Vermote and N. Z. Saleous, "Calibration of NOAA16 AVHRR over a desert site using MODIS data," *Remote Sens. Environ.*, vol. 105, no. 3, pp. 214–220, Dec. 2006.

[25] D. P. Roy, J. Li, H. K. Zhang, L. Yan, H. Huang, and Z. Li, "Examination of Sentinel-2A multi-spectral instrument (MSI) reflectance anisotropy and the suitability of a general method to normalize MSI reflectance to nadir BRDF adjusted reflectance," *Remote Sens. Environ.*, vol. 199, pp. 25–38, Sep. 2017.

[26] H. K. Zhang *et al.*, "Characterization of Sentinel-2A and landsat-8 top of atmosphere, surface, and nadir BRDF adjusted reflectance and NDVI differences," *Remote Sens. Environ.*, vol. 215, pp. 482–494, Sep. 2018.

[27] D. P. Roy *et al.*, "Multi-temporal MODIS–landsat data fusion for relative radiometric normalization, gap filling, and prediction of landsat data," *Remote Sens. Environ.*, vol. 112, no. 6, pp. 3112–3130, Jun. 2008.

[28] Q. Liu, T. Yu, and H. Gao, "Radiometric cross-calibration of GF-1 PMS sensor with a new BRDF model," *Remote Sens.*, vol. 11, no. 6, p. 707, Mar. 2019.

[29] L. Feng, J. Li, W. Gong, X. Zhao, X. Chen, and X. Pang, "Radiometric cross-calibration of Gaofen-1 WFV cameras using Landsat-8 OLI images: A solution for large view angle associated problems," *Remote Sens. Environ.*, vol. 174, pp. 56–68, Mar. 2016.

[30] Z. Wang, X. Xiong, J. Fulbright, and N. Lei, "VIIRS day/night band radiometric calibration stability monitoring using the moon," *J. Geophys. Res., Atmos.*, vol. 122, no. 11, pp. 5616–5624, Jun. 2017.

[31] X. Fan and Y. Liu, "Intercalibrating the MODIS and AVHRR visible bands over homogeneous land surfaces," *IEEE Geosci. Remote Sens. Lett.*, vol. 15, no. 1, pp. 83–87, Jan. 2018.

[32] C. Barrientos, C. Mattar, T. Nakos, and W. Perez, "Radiometric cross-calibration of the chilean satellite FASat-C using RapidEye and EO-1 hyperion data and a simultaneous nadir overpass approach," *Remote Sens.*, vol. 8, no. 7, p. 612, Jul. 2016.

[33] Q. Zheng, Q. Weng, and K. Wang, "Developing a new cross-sensor calibration model for DMSP-OLS and suomi-NPP VIIRS night-light imageries," *ISPRS J. Photogramm. Remote Sens.*, vol. 153, pp. 36–47, Jul. 2019.

[34] L. Yu, Y. Zhang, M. Sun, X. Zhou, and C. Liu, "An auto-adapting global-to-local color balancing method for optical imagery mosaic," *ISPRS J. Photogramm. Remote Sens.*, vol. 132, pp. 1–19, Oct. 2017.

[35] M. Wang, Y. Cheng, X. Chang, S. Jin, and Y. Zhu, "On-orbit geometric calibration and geometric quality assessment for the high-resolution geostationary optical satellite GaoFen4," *ISPRS J. Photogramm. Remote Sens.*, vol. 125, pp. 63–77, Mar. 2017.

[36] Y. Chen, K. Sun, D. Li, T. Bai, and C. Huang, "Radiometric cross-calibration of GF-4 PMS sensor based on assimilation of landsat-8 OLI images," *Remote Sens.*, vol. 9, no. 8, p. 811, Aug. 2017.
[37] M. Wang, Y. Cheng, Y. Tian, L. He, and Y. Wang, "A new on-orbit geometric self-calibration approach for the high-resolution geostationary optical satellite GaoFen4," *IEEE J. Sel. Topics Appl. Earth Observ. Remote Sens.*, vol. 11, no. 5, pp. 1670–1683, May 2018.
[38] J. Liu, G. Zheng, J. Yang, and J. Wang, "Top cloud motion field of typhoon Megi-2016 revealed by GF-4 images," *IEEE Trans. Geosci. Remote Sens.*, vol. 57, no. 7, pp. 4427–4444, Jul. 2019.
[39] J. Wei *et al.*, "An assessment of landsat-8 atmospheric correction schemes and remote sensing reflectance products in coral reefs and coastal turbid waters," *Remote Sens. Environ.*, vol. 215, pp. 18–32, Sep. 2018.
[40] E. Vermote, C. Justice, M. Claverie, and B. Franch, "Preliminary analysis of the performance of the landsat 8/OLI land surface reflectance product," *Remote Sens. Environ.*, vol. 185, pp. 46–56, Nov. 2016.
[41] J. G. Masek *et al.*, "A landsat surface reflectance dataset for North America, 1990–2000," *IEEE Geosci. Remote Sens. Lett.*, vol. 3, no. 1, pp. 68–72, Jan. 2006.
[42] P. Gupta, L. A. Remer, R. C. Levy, and S. Mattoo, "Validation of MODIS 3 km land aerosol optical depth from NASA's EOS Terra and Aqua missions," *Atmos. Meas. Techn.*, vol. 11, no. 5, pp. 3145–3159, May 2018.
[43] R. C. Levy *et al.*, "The collection 6 MODIS aerosol products over land and ocean," *Atmos. Meas. Techn.*, vol. 6, no. 11, pp. 2989–3034, Nov. 2013.
[44] Z. Wang, C. B. Schaaf, Q. Sun, Y. Shuai, and M. O. Román, "Capturing rapid land surface dynamics with collection V006 MODIS BRDF/NBAR/Albedo (MCD43) products," *Remote Sens. Environ.*, vol. 207, pp. 50–64, Mar. 2018.
[45] W. Wanner, X. Li, and A. H. Strahler, "On the derivation of kernels for kernel-driven models of bidirectional reflectance," *J. Geophys. Res., Atmos.*, vol. 100, no. D10, pp. 21077–21089, Oct. 1995.
[46] E. F. Vermote, D. Tanre, J. L. Deuze, M. Herman, and J.-J. Morcette, "Second simulation of the satellite signal in the solar spectrum, 6S: An overview," *IEEE Trans. Geosci. Remote Sens.*, vol. 35, no. 3, pp. 675–686, May 1997.
[47] A. M. Baldridge, S. J. Hook, C. I. Grove, and G. Rivera, "The ASTER spectral library version 2.0," *Remote Sens. Environ.*, vol. 113, no. 4, pp. 711–715, Apr. 2009.
[48] T. He, S. Liang, D. Wang, H. Wu, Y. Yu, and J. Wang, "Estimation of surface albedo and directional reflectance from moderate resolution imaging spectroradiometer (MODIS) observations," *Remote Sens. Environ.*, vol. 119, pp. 286–300, Apr. 2012.
[49] T. He, S. Liang, D. Wang, Q. Shi, and X. Tao, "Estimation of high-resolution land surface shortwave albedo from AVIRIS data," *IEEE J. Sel. Topics Appl. Earth Observ. Remote Sens.*, vol. 7, no. 12, pp. 4919–4928, Dec. 2014.
[50] J. L. Roujean, M. Leroy, and P. Y. Deschamps, "A bidirectional reflectance model of the Earth's surface for the correction of remote sensing data," *J. Geophys. Res. Atmos.*, vol. 97, no. D18, pp. 20455–20468, Dec. 1992.
[51] C. B. Schaaf *et al.*, "First operational BRDF, albedo nadir reflectance products from MODIS," *Remote Sens. Environ.*, vol. 83, nos. 1–2, pp. 135–148, Nov. 2002.
[52] Y. Shuai, J. G. Masek, F. Gao, and C. B. Schaaf, "An algorithm for the retrieval of 30-m snow-free albedo from landsat surface reflectance and MODIS BRDF," *Remote Sens. Environ.*, vol. 115, no. 9, pp. 2204–2216, Sep. 2011.
[53] Y. Shuai, J. G. Masek, F. Gao, C. B. Schaaf, and T. He, "An approach for the long-term 30-m land surface snow-free albedo retrieval from historic landsat surface reflectance and MODIS-based a priori anisotropy knowledge," *Remote Sens. Environ.*, vol. 152, pp. 467–479, Sep. 2014.
[54] F. Gao, T. He, J. G. Masek, Y. Shuai, C. B. Schaaf, and Z. Wang, "Angular effects and correction for medium resolution sensors to support crop monitoring," *IEEE J. Sel. Topics Appl. Earth Observ. Remote Sens.*, vol. 7, no. 11, pp. 4480–4489, Nov. 2014.
[55] B. Franch, E. F. Vermote, and M. Claverie, "Intercomparison of landsat albedo retrieval techniques and evaluation against *in situ* measurements across the US SURFRAD network," *Remote Sens. Environ.*, vol. 152, pp. 627–637, Sep. 2014.
[56] E. Vermote, C. O. Justice, and F.-M. Breon, "Towards a generalized approach for correction of the BRDF effect in MODIS directional reflectances," *IEEE Trans. Geosci. Remote Sens.*, vol. 47, no. 3, pp. 898–908, Mar. 2009.
[57] M. Feng *et al.*, "Global surface reflectance products from landsat: Assessment using coincident MODIS observations," *Remote Sens. Environ.*, vol. 134, pp. 276–293, Jul. 2013.
[58] M. Claverie *et al.*, "Evaluation of medium spatial resolution BRDF-adjustment techniques using multi-angular SPOT4 (take5) acquisitions," *Remote Sens.*, vol. 7, no. 9, pp. 12057–12075, Sep. 2015.
[59] H. Oudrari *et al.*, "Prelaunch radiometric characterization and calibration of the S-NPP VIIRS sensor," *IEEE Trans. Geosci. Remote Sens.*, vol. 53, no. 4, pp. 2195–2210, Apr. 2015.

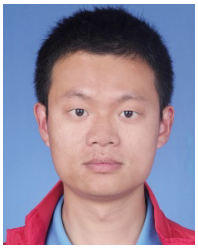

**Jun Lu** received the B.S. degree from Hubei Normal University, Huangshi, China, in 2014, and the M.S. degree from the Innovation Academy for Precision Measurement Science and Technology, Chinese Academy of Sciences (CAS), Wuhan, China, in 2017. He is currently pursuing the Ph.D. degree in photogrammetry and remote sensing with Wuhan University, Wuhan.

His research interest includes remote sensing data radiometric calibration.

**Tao He** (Member, IEEE) received the B.E. degree in photogrammetry and remote sensing from Wuhan University, Wuhan, China, in 2006, and the Ph.D. degree in geography from the University of Maryland, College Park, MD, USA, in 2012.

He is a Professor with the School of Remote Sensing and Information Engineering, Wuhan University, and also with the Department of Geographical Sciences, University of Maryland. His research interests include surface anisotropy and albedo modeling, data fusion of satellite products, and long-term regional and global surface radiation budget analysis.

**Shunlin Liang** (Fellow, IEEE) received the Ph.D. degree from Boston University, Boston, MA, USA.

He is a Professor with the Department of Geographical Sciences, University of Maryland, College Park, MD, USA. He published over 390 SCI indexed peer-reviewed journal article, 42 book chapters, and nine special issues on different journals. He authored/edited seven books and four of which were translated in Chinese, such as "*Quantitative Remote Sensing of Land Surfaces*" (Wiley, 2004), "*Advances in Land Remote Sensing: System, Modeling, Inversion and Application*" (Springer, 2008), "*Advanced Remote Sensing: Terrestrial Information Extraction and Applications*" (Academic Press, 2012, 2019), "*Global LAnd Surface Satellite (GLASS) Products: Algorithms, Validation and Analysis*" (Springer, 2013), "*Land Surface Observation, Modeling and Data Assimilation*" (World Scientific, 2013), and "*Earth's Energy Budget*" (Elsevier, 2017). He has led a team to develop the Global LAns Surface Satellite (GLASS) products that are publically available at (www.glass.umd.edu) and widely used. His main research interests focus on estimating land surface variables from satellite data, global satellite product generation, Earth's energy balance, and environmental changes.

Dr. Liang was the Editor-in-Chief of the nine-volume books titled "*Comprehensive Remote Sensing*" (Elsevier, 2017). He was an Associate Editor of the IEEE TRANSACTIONS ON GEOSCIENCE AND REMOTE SENSING and is currently the Editor-in-Chief of *Science of Remote Sensing*.

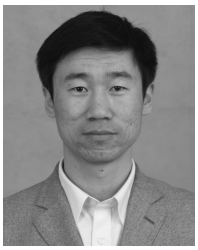

**Yongjun Zhang** was born in 1975. He received the B.S., M.S., and Ph.D. degrees from Wuhan University (WHU), Wuhan, China, in 1997, 2000, and 2002, respectively.

He is currently a Professor of photogrammetry and remote sensing with the School of Remote Sensing and Information Engineering, WHU. His research interests include aerospace and low-attitude photogrammetry, image matching, combined block adjustment with multisource data sets, integration of LiDAR point clouds and images, and 3-D city reconstruction.

Dr. Zhang is the winner of the Second-Class National Science and Technology Progress Award in 2017. He has been supported by the New Century Excellent Talents in University from the Ministry of Education of China in 2007, the China National Science Fund for Excellent Young Scholars in 2013, and the Changjiang Scholars Program from the Ministry of Education of China in 2017.